



Modelling the water distribution within a hydrophilic and hydrophobic 3D reconstructed cathode catalyst layer of a proton exchange membrane fuel cell

T. Hutzenlaub^{a,*}, J. Becker^b, R. Zengerle^a, S. Thiele^a

^a Laboratory for MEMS Applications, IMTEK-Department of Microsystems Engineering, University of Freiburg, Georges-Koehler-Allee 103, 79110 Freiburg, Germany

^b Fraunhofer Institute for Industrial Mathematics (ITWM), Fraunhofer-Platz 1, 67663 Kaiserslautern, Germany

H I G H L I G H T S

- We image, segment and reconstruct a commercial Gore cathode catalyst layer.
- We introduce a method to partially or totally fill the pore space with water.
- We differentiate between a hydrophilic and hydrophobic pore space.
- The method is based on the pore size distribution of the pore space.
- We use the model to calculate parameters accessible surface area and diffusivity.

A R T I C L E I N F O

Article history:

Received 22 June 2012

Received in revised form

22 October 2012

Accepted 20 November 2012

Available online 27 November 2012

Keywords:

Water model

Fuel cell

Cathode

3D reconstruction

Catalyst layer

Bosanquet

A B S T R A C T

We reconstruct a section of the cathode catalyst layer (CCL) of a Gore PEMFC membrane electrode assembly three-dimensionally with nanometre scale resolution. Subsequently, we present a new modelling method to fill the pore space of this matrix stepwise with water, enabling the description of varying saturation conditions of the CCL. The method is based on a 3D pore size distribution and enables to differentiate between a hydrophilic and a hydrophobic CCL. It utilizes a sequence to fill the pores according to their size, going from small to large (hydrophilic) or vice versa (hydrophobic), until a pre-defined value of water saturation is reached. We compare both cases by calculating an effective diffusivity for oxygen in nitrogen in all spatial directions. Both the hydrophilic and the hydrophobic case display a similar ability to transport oxygen up to approximately 50% water saturation of the pore space. At higher water saturation, we calculate larger diffusivity values for the hydrophobic case. Finally, we calculate the specific reaction surface area that is accessible from the gas diffusion layer via unfilled pores for all water saturation conditions. At 50% saturation, the hydrophobic case displays a twenty times larger reaction surface area than the hydrophilic case.

© 2012 Elsevier B.V. All rights reserved.

1. Introduction

Optimized and effective water management is one of the key challenges that remain in proton exchange membrane fuel cell (PEMFC) research, as it influences the performance of nearly all crucial components [1–4]. The ionic conductivity of the membrane depends on membrane hydration. On the one hand, insufficient water saturation of the membrane leads to a higher resistance and thus higher losses, and can cause total failure of the fuel cell due to irreparable damage to the membrane. On the other hand, excessive liquid water will clog both catalyst and gas diffusion layers (GDLs),

slowing gas diffusion to reaction sites significantly. Consequently, establishing and maintaining an optimal balance is mandatory.

As water is produced in the cathode catalyst layer (CCL), flooding is primarily a problem on the cathode side of a PEMFC. While water transport mechanisms in the flow channel, GDL and membrane have been well studied [5–9], the CCL is often approximated as an infinitesimally thin layer. In reality, the CCL is a porous medium with the water-forming reaction occurring throughout the porous network. Models that consider the CCL as a truly spatial structure which is partially saturated with water are still uncommon. Recently, Das et al. formulated a one-dimensional analytical model that allows for the extraction of liquid water profiles, describing water content as a function of layer depth, for both hydrophilic and hydrophobic CCLs [10].

* Corresponding author. Tel.: +49 761 203 73269; fax: +49 761 203 73299.
E-mail address: tobias.hutzenlaub@imtek.de (T. Hutzenlaub).

Nomenclature

A	cross-sectional area of a pore (m^2)
C	circumference of a pore (m)
D_κ	effective Bosanquet diffusivity ($\text{m}^2 \text{s}^{-1}$)
D_k^{bulk}	effective bulk diffusivity ($\text{m}^2 \text{s}^{-1}$)
D_k^{Kn}	effective Knudsen diffusivity ($\text{m}^2 \text{s}^{-1}$)
$D_k^{\text{bulk},0}$	free, substance-specific bulk diffusivity ($\text{m}^2 \text{s}^{-1}$)
$D_k^{\text{Kn},0}$	free, substance-specific Knudsen diffusivity ($\text{m}^2 \text{s}^{-1}$)
$D_k^{\text{bulk},*}$	dimensionless bulk diffusion
$D_k^{\text{Kn},*}$	dimensionless Knudsen diffusion
K	curvature (m^{-1})
Kn	Knudsen number
l	physical length scale of the porous medium involved (m)
p_{cap}	capillary pressure (N m^{-2})
v_{mean}	thermal velocity (m s^{-1})
θ	contact angle ($^\circ$)
κ	subscript defining spatial direction
λ	mean free path (m)
σ	surface tension (N m^{-1})

On the one hand, water in the CCL is necessary to assist proton conduction to reaction sites and is thus beneficial for optimal operation. On the other hand, water-flooded pores will significantly hinder oxygen diffusion to reaction sites and thus have a negative influence on efficiency. In other words, one can assume that there is an optimum water content for the CCL.

Fundamentally, the liquid water content of the CCL is governed by the balance of evaporation and condensation of water as well as the pressure distribution in the porous medium. In the following we only focus on the pressure distribution which can be described by the capillary pressure in the pore network and the pressure on the interfaces between the CCL and membrane, and the CCL and GDL. The capillary pressure p_{cap} at an interface between a gas and a liquid is determined by the Young-Laplace equation:

$$p_{\text{cap}} = \sigma K \quad (1)$$

with the surface tension σ between gas and liquid and the curvature K of the interface. While the surface tension – assuming an approximately homogeneous temperature and material distribution throughout the CCL – is a constant, the curvature varies strongly depending on the actual pore dimensions at the interface location and the contact angle at the associated triple-phase line. Additionally, a porous media usually is not composed of a bundle of unconnected capillaries but instead consists of a complex network of interconnected pores. Accordingly, equilibrium pressure must be established at each intersection, which is influenced by and itself influences all connected pore space. Considering this degree of complexity, it is hardly surprising that until now, only methods that somewhat simplify the structure before offering a solution have been reported. There are many different approaches to accomplish this. In the porous media utilised in fuel cells, these models have mainly been applied to the GDL to date. This includes models that generalize the pore structure (e.g. pore network model [11,12]) or describe the layer with parameters such as effective porosity and permeability [13,14].

In recent years, scanning electron microscopy tomography (SEMT) [15] was utilized to study the microstructure of solid oxide fuel cells (SOFCs). Electrode material was removed layer by layer by a focused ion beam (FIB) and images of each layer were combined

to achieve a three-dimensional reconstruction of the electrodes investigated [16–20]. This method was also applied to lithium-ion batteries [21–23] and PEMFC CCLs [24,25]. In PEMFC CCLs, this allowed for a detailed differentiation of pore and bulk material.

In the reported work, we combine the 3D SEMt reconstruction of a CCL with stepwise filling of the pores with water for both a hydrophilic and a hydrophobic CCL. The method is explained and validated. We investigate how the parameters, diffusivity and accessible surface area, change as the water content increases.

2. Experimental

The cathode of a commercially available Gore PRIMEA A510.1 M710.18C510.4 PEMFC membrane electrode assembly (MEA) was studied with SEMt. Spatial directions are defined as follows and maintained in all further discussion: The z direction is the general translation direction of the FIB whereas the x and y directions define the planes visible in all SEMt images. The y direction indicates the through-plane direction from the interface between the CCL and membrane to the interface between the GDL and CCL (Fig. 1).

A Zeiss 'Neon 40EsB' was used for the SEMt. A $2.5 \times 2.5 \mu\text{m}^2$ platinum protection layer was deposited on top of the porous cathode catalyst layer with a 30 kV acceleration voltage (AV) and a current of 5 pA for 200 s. Two reference lines, one orthogonal and the other with an angle of 55° relative to the cutting plane, were inscribed into the platinum layer with the FIB at 30 kV AV and 50 pA, providing a method to determine slice thickness which is independent of surface skew or irregularities. A cavity, a rectangular prism of dimensions $6 \mu\text{m} \times 4 \mu\text{m} \times 10 \mu\text{m}$ (x , y and z directions), was removed from the sample by FIB milling at 30 kV AV and 500 pA. As a starting point, the sidewall of the cavity in the z direction was finely polished at 30 kV AV and 50 pA. Then the FIB removed a thin layer of the sample in the z direction at 30 kV AV and 50 pA, while the SEM generated an image of every slice between ablation steps at 2 kV AV. The process was subsequently repeated to yield a series of 120 images with an average spacing of 13.6 nm between images and a resolution of 2.5 nm per pixel (Fig. 1). The images were carefully assessed for damage to the cutting plane by either the slicing or imaging step. No indication of deformation on the cutting plane could be detected. The pore walls behind the cutting plane, visible due to the depth of focus, displayed no change in morphology between successive images. While a small degree of distortion can't be ruled out due to FIB/SEM being an invasive method, this error is thus judged to be negligible.

The complete experimental reconstruction procedure of the SEMt including alignment was performed according to the approach described in [21,25]. The segmentation was accomplished semi-automatically by first applying a threshold and then manually correcting the images.

Methods such as calculating the pore-size distribution according to the approach employed in this work demand cubic voxels. Accordingly, the resolution of the x and y direction was first rescaled to $3.4 \text{ nm} \times 3.4 \text{ nm}$ by linear interpolation, resulting in a voxel size of $3.4 \text{ nm} \times 3.4 \text{ nm} \times 13.6 \text{ nm}$. Then each voxel was divided into 4 sub-voxels measuring $3.4 \text{ nm} \times 3.4 \text{ nm} \times 3.4 \text{ nm}$. The final geometry was cropped to a cube of $1.632 \mu\text{m} \times 1.632 \mu\text{m} \times 1.632 \mu\text{m}$ and $480 \times 480 \times 480$ voxels. A preliminary porosity of 58.08% was calculated.

On every image, small non-connected areas attributed to errors during the semi-automatic segmentation process were eliminated from both the solid and porous phases. This was performed by applying the `bwareaopen` function in Matlab [26] in 2D which removed all non-connected 2D particles with a size smaller than 10 pixels set to an 8-connected neighbourhood (all pixels that share an

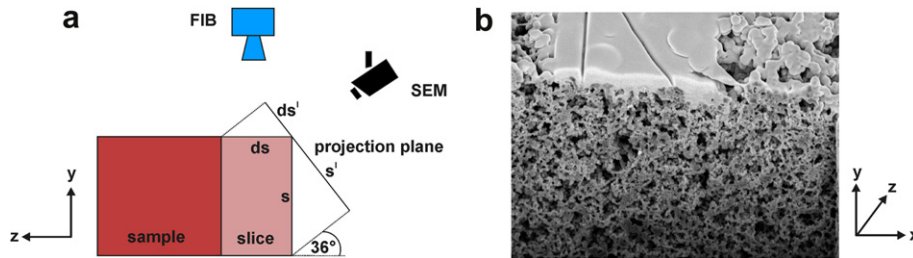


Fig. 1. a) Schematic diagram of the experimental set-up. A small sample of a PEMFC cathode is ablated slice by slice with a focused ion beam. A scanning electron microscope angled at 36° relative to the sample surface plane creates one image per slice. Schematic as published in [21]. b) One of the images recorded between ablation steps. The cutting plane and sample surface with two reference lines imprinted into a deposited platinum layer for the alignment process are visible. Due to the camera angle, images must be aligned.

edge or vertex are defined as connected). The result is an intermediate porosity of 58.12%.

The `bwconncomp` function in Matlab [26] was used in 3D to remove small non-connected 3D areas and evaluate differences in 3D connectivity. This was performed by the following steps for a 6-connected (voxels must share a face to be connected), 18-connected (voxels must either share a face or edge to be connected) and 26-connected (voxels must either share a face, edge or vertex to be connected) neighbourhood respectively:

- The largest connected solid region in the 3D geometry is identified. Depending on connectivity definition, this region consists of 98.78% (6-connected), 98.80% (18-connected) and 98.80% (26-connected) of the voxels defined as solid in the geometry.
- All other solid regions not connected to this largest region are converted to pore space.
- The largest connected pore in the 3D geometry is identified. Depending on connectivity definition, this pore consists of between 99.88% (6-connected), 99.90% (18-connected) and 99.91% (26-connected) of the voxels defined as pore in the geometry.
- All other pores not connected to this largest pore are converted to solid.

The results are porosities of 58.14% (6-connected), 58.15% (18-connected) and 58.15% (26-connected). The 6-connected porous 3D matrix was chosen as starting point for all further investigations (Fig. 2).

3. Mechanism of water filling

One of the most important parameters for characterising a partially flooded porous medium is the wettability of the pore walls. Due to the small dimensions of the CCL, measuring an internal contact angle is not yet feasible. Most authors characterise the catalyst layer by placing a static droplet on the surface of a CCL to gain at least a general indication concerning the wettability [27–31]. The disadvantage of this approximation is that there is no guarantee that the generated values are applicable to the pore space consisting of pores on a totally different scale. Additionally, a certain amount of contact angle hysteresis is to be expected, further increasing the possible error. To reduce this uncertainty, we consider the equation first introduced by Finn [32]:

$$\int_A p_{\text{cap}} = \int_C \sigma \cos \theta \quad (2)$$

where the capillary pressure p_{cap} over an interface can be calculated with the contact angle θ along the circumference C and the cross-

sectional area A without knowledge of the exact interface shape. At $\theta = 90^\circ$, the capillary pressure changes sign, thus altering the fundamental behaviour concerning where liquid water will preferably reside to minimize pressure. In other words, in the hydrophilic case, small pores will primarily fill with water; in the hydrophobic case, the larger pores will be more attractive to water. Our model describes these two different cases.

A three-dimensional pore size distribution (PSD) naturally contains information that differentiates between different sizes of pores. Consequently we model the fundamental behaviour of hydrophilic and hydrophobic water filling by first calculating a spatially resolved PSD and then gradually filling the pore space with water. This water filling depends solely on pore size. In the hydrophilic case the smallest pores are filled first and then larger and larger pores are filled until a predefined threshold of water saturation is reached (Fig. 3). This was performed in 10% steps of total pore volume, until all pore space is filled. In the hydrophobic case, the mechanism is inverted. The largest pores are filled first and then smaller and smaller pores are filled up to a predefined threshold. This was also performed in 10% steps of pore space total pore volume, until all pore space is filled. To accomplish this, we use an adaptation of the approach which was described in reference [33] and further developed in reference [25]. In a first step, every voxel belonging to the pore space of the 3D reconstruction matrix is identified. Then the distance to the nearest pore wall is calculated. Spheres with a radius of this minimum distance are inscribed into each voxel of the pore space, with larger spheres overwriting

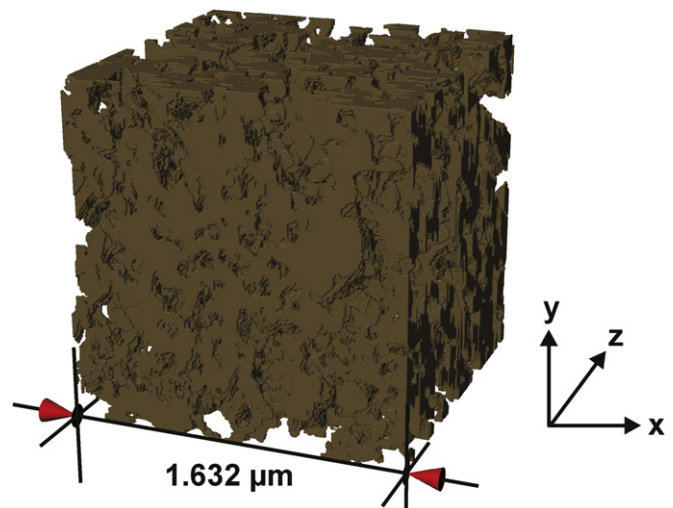


Fig. 2. Visualization of the 3D reconstruction of a PEMFC cathode used as starting point for water modelling in the reported work. The cubic representation of the bulk phase measures 1.632 μm along each edge.

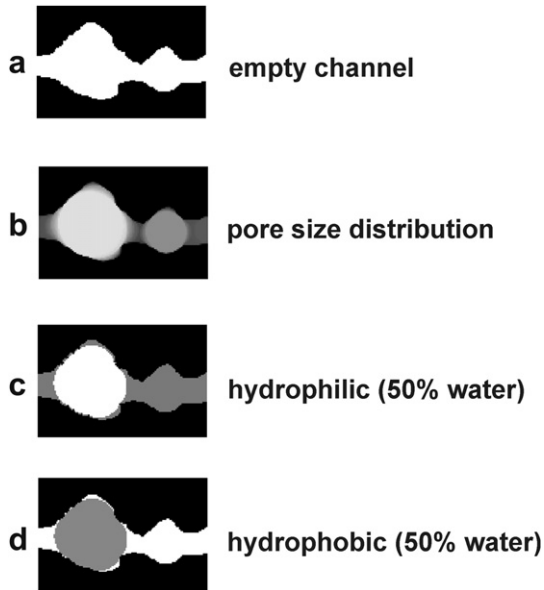


Fig. 3. a) Empty channel (white = pore, black = bulk). b) Spheres inscribed into the pore as a measure for the pore size distribution (PSD). Smaller spheres are depicted in darker grey. Larger spheres overwrite smaller spheres. c) Hydrophilic pore with a water saturation of 50% (white = pore, black = bulk, grey = water). Small spheres of the PSD are filled first. d) Hydrophobic pore with a water saturation of 50% (white = pore, black = bulk, grey = water). Large spheres of the PSD are filled first.

smaller spheres. This avoids unphysical gaps between spheres, as would occur in a packing of spheres without overlap. A grey-scale value of 100 describing water (with 0 – black – and 255 – white – depicting pore and bulk material respectively) is assigned to this resulting set of spheres. The geometry is filled in 10% steps of pore volume from smallest to largest (hydrophilic case) or largest to smallest (hydrophobic case) (Fig. 4, Fig. 5). To verify the method, a PSD [25,33] of the remaining pore space is calculated with GeoDict [34] and depicted in Fig. 6. The stepwise water flooding was implemented in Matlab [26].

This three-dimensional PSD water model does not consider water transport dynamics, such as contact angle hysteresis, or the possibility of capillary stops due to a varying pore radius along a capillary. However, we describe an important base case where the surface energy of the geometry is at its minimum for a specific

degree of water saturation. This procedure lets us take full advantage of the 3D reconstruction of the real microstructure presented in this work for the calculations of parameters in dependence on water content, without having to simplify pore structure.

4. Characterization of the partially filled 3D reconstruction

The diffusion rate of oxygen in air is approximately 10^5 times higher than in water [35]. As a result, we assume that only the pores that are not filled with water contribute to the oxygen supply of the catalyst layer. This allows us to graphically add the water phase to the bulk phase for every degree of water saturation of our 3D reconstruction, with the colour black describing pore space and the colour white depicting the sum of water and bulk phase, thus significantly reducing calculation time for the following calculations.

4.1. Calculation of gas diffusivity values in dependence on water saturation

The appropriate diffusion mechanism in a porous medium is determined by the Knudsen number Kn :

$$Kn = \frac{\lambda}{l} \quad (3)$$

λ is defined as the mean free path between two successive intermolecular collision events and is a specific value for a given gas at a constant pressure and temperature. l describes a representative geometric physical length scale of the porous medium involved, which is typically, but not necessarily, an average pore diameter. If this physical length scale is much smaller than λ , Kn will become very large and instead of intermolecular collisions, molecules will predominantly collide with pore walls. This type of diffusion is called Knudsen diffusion and can be modelled by a random walk approach [36–38].

For small Knudsen numbers, diffusion mainly occurs due to collisions between molecules. This type of diffusion is called bulk diffusion and is typically modelled by the well-known continuum mechanics approach.

At intermediate Knudsen numbers, as are applicable to the reconstructed CCL, both intermolecular and molecule-wall collisions contribute significantly. In this case, the overall effective diffusivity can be approximated by Bosanquet's formula [37,39]:

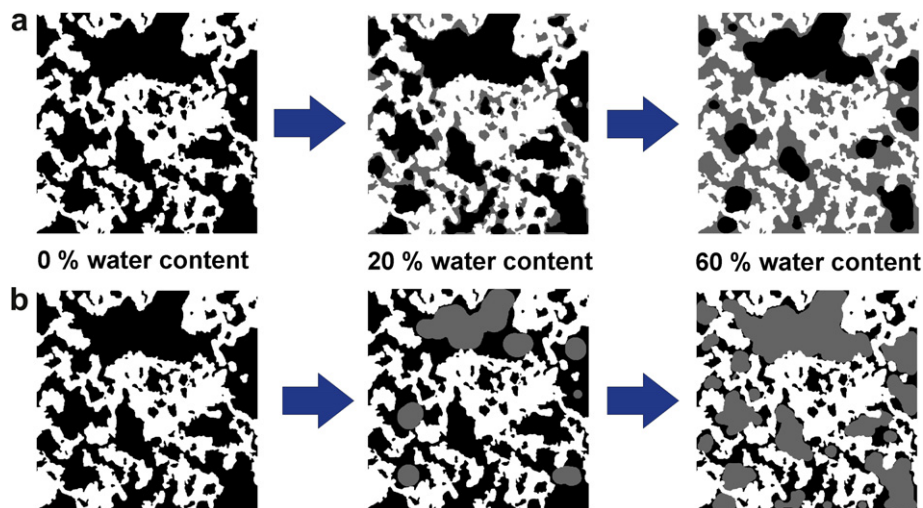


Fig. 4. 2D sectional view of 0.2 μm edge length in z direction for varying filling levels. a) 0%, 20% and 60% water content of a hydrophilic 3D reconstruction. b) 0%, 20% and 60% water content of a hydrophobic 3D reconstruction.

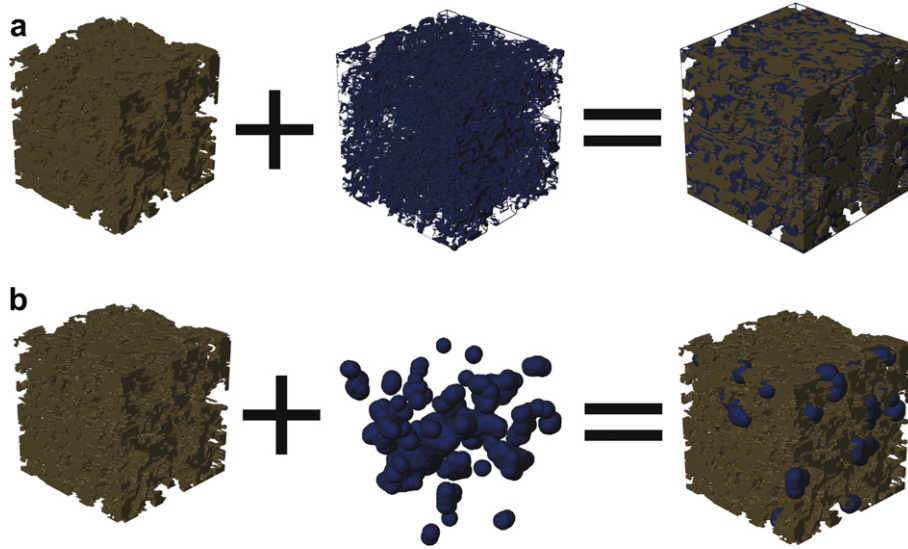


Fig. 5. Visualization of a partially filled 3D reconstruction. 20% of the pore space is filled with water (blue). a) Hydrophilic case, small pores are filled first. b) Hydrophobic case, large pores are filled first. (For interpretation of the references to colour in this figure legend, the reader is referred to the web version of this article.)

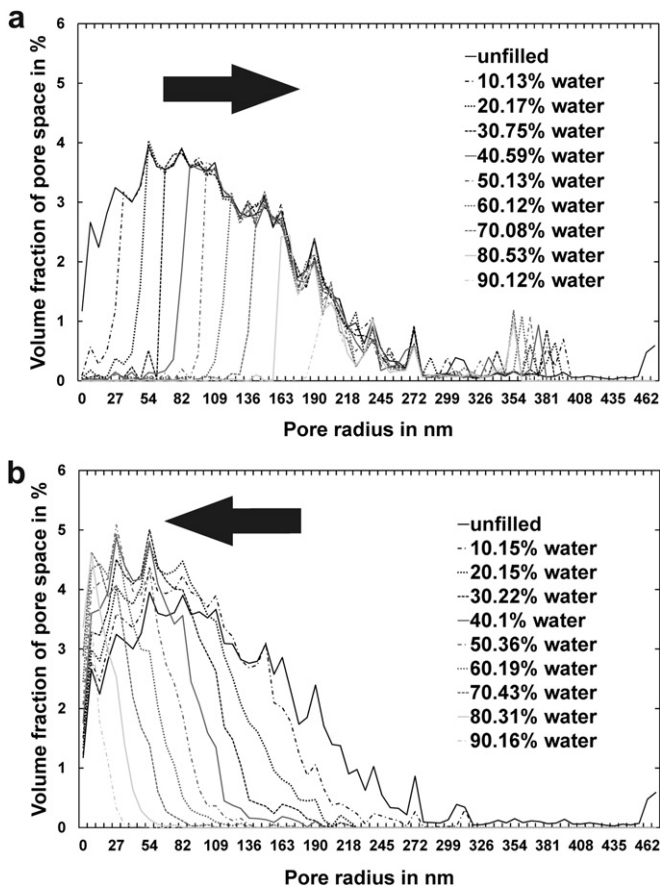


Fig. 6. Pore size distribution (PSD) of the remaining pore space at varying filling levels. a) Hydrophilic filling; small pores are filled first. Accordingly, the PSD distribution is cropped stepwise from left to right. Irregularities are due to edge effects at the interface between water, solid and gas, thus creating additional possibilities to inscribe small spheres due to the curvature near the triple-phase line. b) Hydrophobic filling; large pores are filled first. Accordingly, the PSD distribution is cropped stepwise from right to left. Irregularities are due to edge effects at the interface between water, solid and gas, thus creating additional possibilities to inscribe small spheres due to the curvature near the triple-phase line.

$$D_{\kappa} = \left((D_{\kappa}^{Kn})^{-1} + (D_{\kappa}^{bulk})^{-1} \right)^{-1} \quad \kappa = x, y, z \quad (4)$$

Both the effective bulk diffusivity D_{κ}^{bulk} and the effective Knudsen diffusivity D_{κ}^{Kn} can be understood as the result of dimensionless diffusivity matrices $D_{\kappa}^{bulk,*}$ and $D_{\kappa}^{Kn,*}$, depending only on the geometry of the porous media, multiplied by free, substance-specific diffusivity values $D^{bulk,0}$ and $D^{Kn,0}$, respectively.

$$D_{\kappa}^{bulk} = D_{\kappa}^{bulk,*} D^{bulk,0} \quad \kappa = x, y, z \quad (5)$$

$$D_{\kappa}^{Kn} = D_{\kappa}^{Kn,*} D^{Kn,0} \quad \kappa = x, y, z \quad (6)$$

$D_{\kappa}^{bulk,*}$ and $D_{\kappa}^{Kn,*}$ are calculated as described by Becker et al. [37] with GeoDict [34], where $D_{\kappa}^{bulk,*}$ is the result of solving Fick's law and $D_{\kappa}^{Kn,*}$ is derived by utilizing a random walk approach. $D_{\kappa}^{bulk,*}$, $D_{\kappa}^{Kn,*}$ and the characteristic length l which is the average distance between molecule-wall collisions and is the result of the random walk simulation are depicted in Figs. 7–9. $D^{bulk,0}$ is defined as either the self-diffusion coefficient of a pure gas or in the case of a binary gas mixture such as oxygen in nitrogen as we can assume in the CCL the measurable diffusion coefficient in free space. At standard conditions (25 °C, 191.3 kPa) $D^{bulk,0} = 20.86 \text{ mm}^2 \text{ s}^{-1}$ [37]. $D^{Kn,0}$ is given by:

$$D^{Kn,0} = \frac{1}{3} l v_{\text{mean}} \quad (7)$$

At standard conditions the mean thermal velocity is $v_{\text{mean}} = 444.1 \text{ m s}^{-1}$ [37]. Thus we are now able to determine the effective diffusivity coefficient D_{κ} of oxygen in nitrogen in the CCL in dependence on the water content of the pores with Bosanquet's formula. The result is depicted in Fig. 10.

Both the hydrophilic and the hydrophobic case display a similar ability to transport oxygen up to approximately 50% water saturation of the pore space. At higher water saturation, we calculate larger diffusivity values for the hydrophobic case. The pore space in the hydrophilic case is entirely blocked at approximately 70% water saturation. In the hydrophobic case, connectivity through the sample is provided up to a value of approximately 90% water saturation.

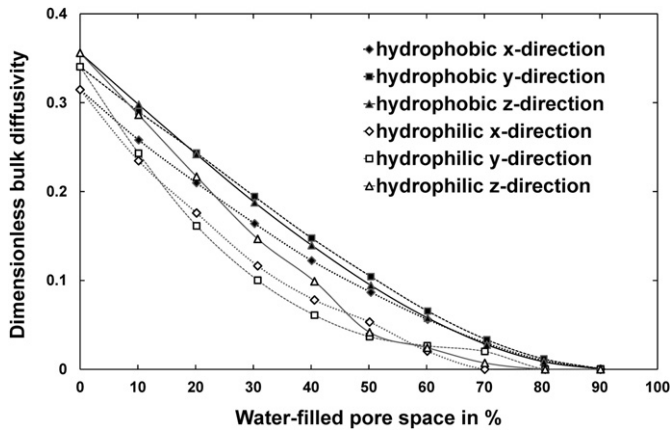


Fig. 7. Dimensionless bulk diffusivity in all spatial directions for both the hydrophilic and the hydrophobic cases. Connecting lines between data points are added for better visibility.

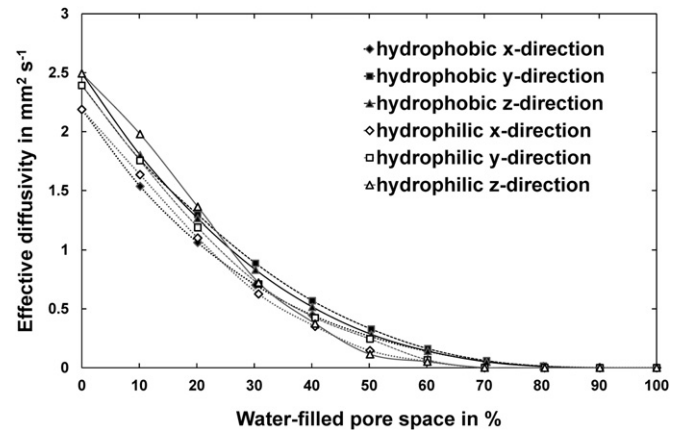


Fig. 10. Effective diffusivity in all spatial directions for both the hydrophilic and the hydrophobic cases. In the hydrophilic case, diffusion through the reconstructed section comes to a complete standstill at approximately 70% water content in the pore space. In the hydrophobic case, diffusion through the reconstructed section is possible until approximately 90% water content. For both cases all three spatial directions yield similar results. Connecting lines between data points are added for better visibility.

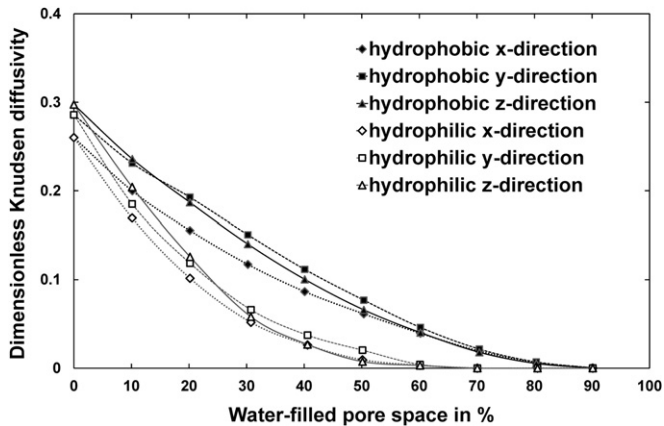


Fig. 8. Dimensionless Knudsen diffusivity in all spatial directions for both the hydrophilic and the hydrophobic cases. Connecting lines between data points are added for better visibility.

4.2. Calculation of specific GDL-connected surface area in dependence on water saturation

In general, the effective diffusivity in all spatial directions gives a good indication of how the reconstructed part of the CCL

contributes to blockage or passage of oxygen in dependence on water saturation, thus characterising its degree of connectivity. However, this is not an exact measure of how the CCL-represented by the reconstructed 3D cube—losses reactivity as the water content rises. To quantify this, one can assume that the most important path for oxygen diffusion is from the GDL side into the CCL. Thus, we fill all pores that are not connected to this side of the reconstructed 3D geometry with bulk material by a tool based on the `bwconncomp` function in Matlab [26] and then calculate the remaining surface area that is not covered by water. The surface area calculation was performed by employing a method first introduced by Ohser et al. [40] with GeoDict [34] (Fig. 11) for both the hydrophilic and the hydrophobic cases at varying values of water saturation. This surface area is related to the volume of the 3D reconstruction to determine a specific surface area that is available for reaction. The hydrophobic case demonstrates considerably higher tolerance to water saturation. At 50% saturation, we calculate a specific reaction surface area that is approximately twenty times higher than for the hydrophilic case.

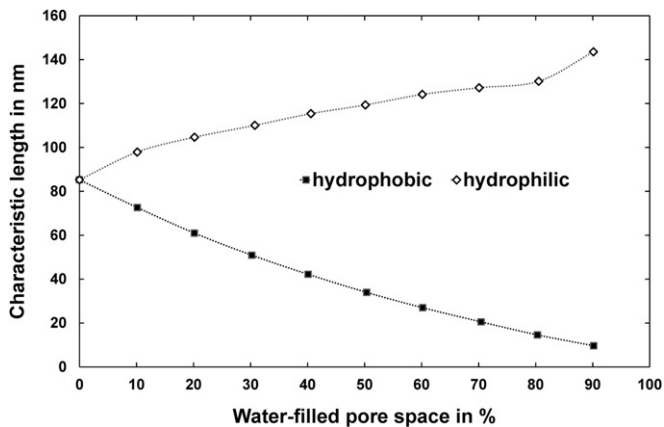


Fig. 9. The characteristic length for both the hydrophilic and the hydrophobic cases. It is defined as the average distance between molecule-wall collisions and is the result of the random walk simulation. Connecting lines between data points are added for better visibility.

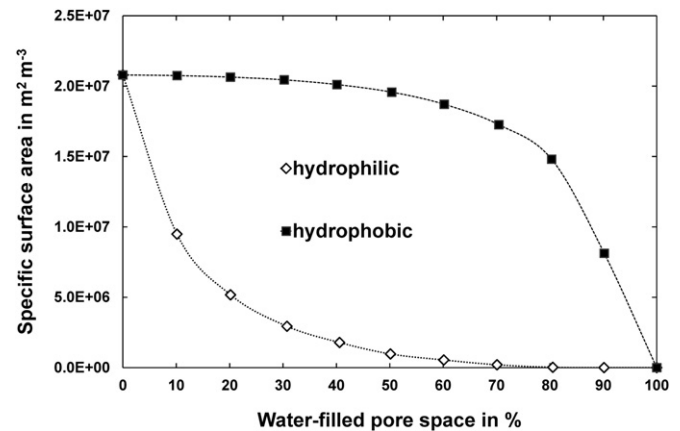


Fig. 11. Specific surface area connected to the gas diffusion layer side of the reconstructed sample via pore space that is not filled with water. At 50% saturation, the specific reaction surface area is approximately twenty times higher than for the hydrophilic case. Connecting lines between data points are added for better visibility.

5. Conclusion and outlook

Firstly, we successfully demonstrated a mechanism to partially fill a 3D reconstruction of a porous medium with water, without needing to streamline the geometry to a more calculation-friendly configuration such as packed spheres. This is valuable to achieve a more realistic starting point for porous media simulations.

Secondly, we compared a hydrophilic and a hydrophobic CCL by calculating an effective diffusivity of oxygen in nitrogen and a specific, GDL-connected surface area. While diffusivity values of both cases are similar, the surface area strongly favours a hydrophobic CCL as the layer that is expected to produce higher power densities, due to better accessibility of the catalyst for oxygen.

Comparison of the proton conductivity for the two configurations is still an object for future research.

The water-filled 3D reconstruction presented in this publication can be provided on request.

Acknowledgements

This work is part of the project PEM-Ca-D (Grant No. 03SF0360D) and is funded by the German Ministry of Education and Research (BMBF).

References

- [1] H. Li, Y.H. Tang, Z.W. Wang, Z. Shi, S.H. Wu, D.T. Song, J.L. Zhang, K. Fatih, J.J. Zhang, H.J. Wang, Z.S. Liu, R. Abouatallah, A. Mazza, *Journal of Power Sources* 178 (2008) 103–117.
- [2] W. Schmittinger, A. Vahidi, *Journal of Power Sources* 180 (2008) 1–14.
- [3] J.P. Owejan, J.J. Gagliardo, J.M. Sergi, S.G. Kandlikar, T.A. Trabold, *International Journal of Hydrogen Energy* 34 (2009) 3436–3444.
- [4] Z. Lu, S.G. Kandlikar, C. Rath, M. Grimm, W. Domigan, A.D. White, M. Hardbarger, J.P. Owejan, T.A. Trabold, *International Journal of Hydrogen Energy* 34 (2009) 3445–3456.
- [5] T.V. Nguyen, R.E. White, *Journal of the Electrochemical Society* 140 (1993) 2178–2186.
- [6] Z.H. Wang, C.Y. Wang, K.S. Chen, *Journal of Power Sources* 94 (2001) 40–50.
- [7] L.Y. You, H.T. Liu, *International Journal of Heat and Mass Transfer* 45 (2002) 2277–2287.
- [8] J.S. Yi, T.V. Nguyen, *Journal of the Electrochemical Society* 145 (1998) 1149–1159.
- [9] S. Dutta, S. Shimpalee, J.W. Van Zee, *International Journal of Heat and Mass Transfer* 44 (2001) 2029–2042.
- [10] P.K. Das, X.G. Li, Z.S. Liu, *International Journal of Hydrogen Energy* 35 (2010) 2403–2416.
- [11] J.T. Gostick, M.A. Ioannidis, M.W. Fowler, M.D. Pritzker, *Journal of Power Sources* 173 (2007) 277–290.
- [12] P.K. Sinha, C.Y. Wang, *Electrochimica Acta* 52 (2007) 7936–7945.
- [13] U. Pasaogullari, P.P. Mukherjee, C.Y. Wang, K.S. Chen, *Journal of Electrochemical Society* 154 (2007) B823–B834.
- [14] H. Ju, G. Luo, C.Y. Wang, *Journal of the Electrochemical Society* 154 (2007) B218–B228.
- [15] L. Holzer, F. Indutnyi, P.H. Gasser, B. Munch, M. Wegmann, *Journal of Microscopy* 216 (2004) 84–95.
- [16] J.R. Wilson, W. Kobsiriphat, R. Menziona, H.Y. Chen, J.M. Hiller, D.J. Miller, K. Thornton, P.W. Voorhees, S.B. Adler, S.A. Barnett, *Natural Materials* 5 (2006) 541–544.
- [17] J. Joos, T. Carraro, A. Weber, E. Ivers-Tiffée, *Journal of Power Sources* 196 (2011) 7302–7307.
- [18] D. Gostovic, J.R. Smith, D.P. Kunder, K.S. Jones, E.D. Wachsman, *Electrochemical and Solid-State Letters* 10 (2007) B214–B217.
- [19] J.R. Wilson, A.T. Duong, M. Gameiro, H.Y. Chen, K. Thornton, D.R. Mumm, S.A. Barnett, *Electrochemistry Communications* 11 (2009) 1052–1056.
- [20] J.R. Wilson, J.S. Cronin, A.T. Duong, S. Rukes, H.Y. Chen, K. Thornton, D.R. Mumm, S. Barnett, *Journal of Power Sources* 195 (2010) 1829–1840.
- [21] T. Hutzenlaub, S. Thiele, R. Zengerle, C. Ziegler, *Electrochemical and Solid-State Letters* 15 (2012) A33–A36.
- [22] J.R. Wilson, J.S. Cronin, S.A. Barnett, S.J. Harris, *Journal of Power Sources* 196 (2011) 3443–3447.
- [23] M. Ender, J. Joos, T. Carraro, E. Ivers-Tiffée, *Electrochemistry Communications* 13 (2011) 166–168.
- [24] C. Ziegler, S. Thiele, R. Zengerle, *Journal of Power Sources* 196 (2011) 2094–2097.
- [25] S. Thiele, R. Zengerle, C. Ziegler, *Nano Research* 4 (2011) 849–860.
- [26] www.mathworks.com, 2012.
- [27] Z.L. Miao, H.M. Yu, W. Song, D. Zhao, L.X. Hao, B.L. Yi, Z.G. Shao, *Electrochemistry Communications* 11 (2009) 787–790.
- [28] W. Song, H.M. Yu, L.X. Hao, Z.L. Miao, B.L. Yi, Z.G. Shao, *Solid State Ionics* 181 (2010) 453–458.
- [29] A.D. Li, M. Han, S.H. Chan, N.T. Nguyen, *Electrochimica Acta* 55 (2010) 2706–2711.
- [30] U.H. Jung, K.T. Park, E.H. Park, S.H. Kim, *Journal of Power Sources* 159 (2006) 529–532.
- [31] K.H. Oh, W.K. Kim, K.A. Sung, M.J. Choo, K.W. Nam, J.W. Choi, J.K. Park, *International Journal of Hydrogen Energy* 36 (2011) 13695–13702.
- [32] R. Finn, *Equilibrium Capillary Surfaces*, Springer-Verlag, Stanford, 1986.
- [33] J.F. Delerue, E. Perrier, Z.Y. Yu, B. Velde, *Physics and Chemistry of the Earth Part A – Solid Earth and Geodesy* 24 (1999) 639–644.
- [34] www.geodict.com, 2012.
- [35] E.L. Cussler, *Diffusion: Mass Transfer in Fluid Systems*, Cambridge University Press, 2009.
- [36] H. Babovsky, *Journal of Statistical Physics* 44 (1986) 865–878.
- [37] J. Becker, C. Wieser, S. Fell, K. Steiner, *International Journal of Heat and Mass Transfer* 54 (2011) 1360–1368.
- [38] A. Berson, H.W. Choi, J.G. Pharoah, *Physical Review E* 83 (2011) 026310.
- [39] W.G. Pollard, R.D. Present, *Physical Review* 73 (1948) 762–774.
- [40] J. Ohser, F. Muecklich, *Statistical Analysis*, Wiley & Sons, 2000.